



Towards high-throughput large-area metalens fabrication using UV-nanoimprint lithography and Bosch deep reactive ion etching

CHRISTOPHER A. DIRDAL, *  GEIR URI JENSEN, HALLVARD ANGELSKÅR, PAUL CONRAD VAAGEN THRANE, JO GJESSING, AND DANIEL ALFRED ORDNING

SINTEF Microsystems and Nanotechnology, Gaustadalleen 23C, 0737 Oslo, Norway
*christopher.dirdal@sintef.no

Abstract: We demonstrate the fabrication of diffraction-limited dielectric metasurface lenses for NIR by the use of standard industrial high-throughput silicon processing techniques: UV nano imprint lithography (UV-NIL) combined with continuous reactive ion etching (RIE) and pulsed Bosch deep reactive ion etching (DRIE). As the research field of metasurfaces moves towards applications, these techniques are relevant as potential replacements of commonly used cost-intensive fabrication methods utilizing electron beam lithography. We show that washboard-type sidewall surface roughness arising from the Bosch DRIE process can be compensated for in the design of the metasurface, without deteriorating lens quality. Particular attention is given to fabrication challenges that must be overcome towards high-throughput production of relevance to commercial applications. Lens efficiencies are measured to be 25.5% and 29.2% at wavelengths $\lambda = 1.55\mu\text{m}$ and $\lambda = 1.31\mu\text{m}$, respectively. A number of routes towards process optimization are proposed in relation to encountered challenges.

© 2020 Optical Society of America under the terms of the [OSA Open Access Publishing Agreement](#)

1. Introduction

1.1. Challenging the paradigm for optical sensor design

The current revolution in sensor technologies is opening up for a wide number of new applications where optical components are required to be *small, lightweight and cheap*, without compromise on optical quality. A significant drawback for optical sensor technology in this context, however, is the fact that optical systems are generally *big, heavy, and expensive*. The recent developments within nanopatterning techniques and simulation tools have led to the development of the research field known as *metasurfaces* which may challenge this paradigm. Metasurfaces may do so by allowing to fabricate optics using the same standard silicon (Si) processing technology used to fabricate electronics. Although there currently do exist lithographical methods to make e.g. high quality curved microlenses, metasurfaces offer the advantage of being able to integrate a multitude of optical functions (e.g. lens, filter, polarizer) into a single surface. In this respect, metasurfaces have many similarities with diffractive optical elements. However, by utilizing optical resonances in nanostructures such as pillars, bricks or discs (rather than e.g. stepped gratings) metasurfaces offer unprecedented control over all degrees of freedom of the propagating field: The phase, intensity, polarization and dispersion. Furthermore metasurfaces can potentially be integrated into the same Si process lines which already are used for making e.g. detectors or optical MEMS components. This is a development with significant potential to save costs and reduce sizes. For instance in the context of photodetectors, the microlenses and detectors generally rely on separate manufacturing lines, while the integration of metasurfaces either by deep ultraviolet lithography or potentially also compatible UV-NIL processes would allow this in the same manufacturing line.

1.2. Towards high-throughput, large-area patterning

As the research field has until now been primarily interested in demonstrating the potential of metasurfaces, most dielectric metasurface lenses (or *metalenses*) are fabricated by using the best resolution nanopatterning methodologies, despite tending to be slow and costly. To be more specific, virtually every paper on state-of-the-art dielectric metalenses to date has relied on Electron Beam Lithography (EBL) [1–9]. Here EBL is typically used in one of two ways: (i) EBL is used to pattern resist for a metal lift-off, thereby attaining a hard mask for subsequent etching of the (typically silicon) metasurface structures (typically for operation in NIR, but also VIS) [1–5], or (ii) EBL is used to pattern high aspect ratio resist (as much as 15:1) holes for subsequent ALD deposition of TiO₂ which, after lift-off, yield the metasurface structures (typically for operation in VIS) [6–9]). The latter technique is typically used when extreme structural requirements apply, such as for minimum gaps between metasurface pillars being less than 20nm. Moving on towards applications, it is therefore necessary to develop low cost, high-throughput, large-area patterning methods (as agreed upon in [10–16]) which at the same time offer comparable reproducibility and resolution as to that of EBL.

Several fabrication methods relevant to large-area patterning have been proposed and partially applied to metasurfaces [13,14], including nanoimprint lithography [17–32] which is the topic of this paper, and immersion deep ultraviolet lithography [33–35]. The latter has particularly been investigated as a promising candidate for high-volume fabrication of metalenses in relation to CMOS-compatible detector fabrication. Although this technique provides sub 100 nm resolution and excellent critical dimension tolerances, the equipment investment cost is prohibitive for many fabs. In addition, nanoimprint lithography will likely be more suitable for wafers with significant surface topography (especially relevant for MEMS fabrication) and can also be used to directly imprint complex 3D patterns which are not possible with traditional or immersion photolithography. For slightly larger feature sizes (e.g. 250 nm), deep ultraviolet stepper lithography is promising for high-throughput fabrication, see e.g [16,36]. Other techniques that may be mentioned are interference lithography [37], plasmonic lithography [10,38], pattern transfer [39,40], additive manufacturing [41], self-assembly [21,42,43], and associated high-throughput roll-to-roll and stepping processes [44]. Examples of NIL applied to non-lensing metasurface applications include Mie-resonant holes and line-structures for photoluminescence enhancement control [17,18], line structures for unidirectional transmission [19], colloidal Au nanocrystals acting as quarter wave plates [20] and chemically tailored dielectric-to-metal transition surfaces [21], metallic nano-woodpiles (Moiré patterns) for photonic crystal bandgaps [22,23], metal-dielectric stacked fishnet structures for negative index metamaterials [24–26], plasmonic structures for active tuning colour [27], localized surface plasmon resonance control [28], plasmonic photonic crystal lattice acting as a plasmonic absorber [29], and line structures which act as cylindrical beam generators [30].

Despite the wide variety of publications on nanoimprint lithography applied to metasurfaces just mentioned, there are to our knowledge only a few examples in which dielectric metalenses have been made using nanoimprint [31,32]. This is possibly explained by the challenges involved for etching quality structures with vertical sidewalls and aspect ratios ranging between 2:1 to 15:1. Also, as mentioned above, for demonstrations and "proof of principle" prototypes, the time required by direct writing methods such as Electron Beam Lithography (EBL) is not critical. Nevertheless, transitioning into technological applications, this challenge must be addressed. The authors of [32] found that using a classical parallel-plate Reactive Ion Etch (RIE) with a metallic mask yielded slanted sidewalls in the metasurface structures, which in turn seem likely to have reduced the optical quality of their lens. An alternative approach based on selective area sublimation was used to overcome this issue (but which is only applicable to crystalline materials). In [31] metalenses of good optical quality are reported, fabricated by evaporating a stack of SiO₂, Cr and Au onto a polymer stamp, after which the stack is transferred to a Si film on

quartz substrate by imprinting. The de-attached SiO₂-Cr-Au stack is then used as an etch mask for the Si film. This method has the advantage of avoiding the need to pattern the hard mask through etching, but it seems likely that the polymer stamp must be cleaned or re-created for every imprint.

1.3. Our contribution

In this paper we present the utilization of standard industrial high-throughput silicon processing techniques for the fabrication of diffraction-limited dielectric metasurface lenses for NIR: We have used UV Nano Imprint Lithography (UV-NIL) patterning of a resist mask with subsequent Continuous and Bosch Deep Reactive Ion Etching (DRIE) for fabricating quality metastructures with vertical sidewalls. To our knowledge this is the first such demonstration of the combination of these techniques, which are highly relevant to the growing demand for developing high-throughput, large-area patterning techniques for dielectric metasurfaces. We discuss how the characteristic "washboard" sidewall surface roughness arising from the Bosch process does not reduce optical quality of the metalens when adopting a simple compensation strategy (Sec. 2.3), and we provide a discussion of the Bosch DRIE method in Sec. 4.2 relative to other possible etch contenders for high-throughput production. We present a detailed account of the processing steps and the challenges involved, in order to hopefully contribute to the advancement of UV-NIL and DRIE as a route to achieve this. Employing UV-NIL still requires the fabrication of a master wafer, typically using EBL, but the cost of this can be reduced by fabricating masters with single (or several) dies, which are replicated to pattern a full master wafer using stepper nanoimprint lithography (stepper NIL) and reactive ion etching. However, full-wafer patterning by stepper NIL is not addressed in this paper.

2. Design of metalens

2.1. Physical principle

The optical design of the metasurfaces relies on dielectric rectangular pillar arrays (Fig. 2(b)) and the widely used geometric phase principle [7,9,45,46].

The phase function $\phi(r)$ of a lens (which focuses normally incident light to a focal point a distance f from the center of the lens) is given by

$$\phi(r) = \frac{2\pi}{\lambda} \left(\sqrt{r^2 + f^2} - f \right). \quad (1)$$

where λ is the wavelength of interest and r is the radial distance from the center. The job of the metalens is to add the phase amount $\phi(r)$ to the incoming field at each point r on the metasurface. If the incoming field is circularly polarized, phase can be added to the field by transmitting it through rotated rectangular pillars on the metasurface, rotated by an angle

$$\alpha(r) = \phi(r)/2, \quad (2)$$

as sketched in Fig. 1(a). This is known as the *geometric phase principle*, in which the transmitted field $|E_{\text{out}}\rangle$ may be expressed as

$$|E_{\text{out}}\rangle = \frac{t_x + t_y}{2} |L\rangle + \frac{t_x - t_y}{2} \exp(i\phi) |R\rangle, \quad (3)$$

where we have assumed that the incoming field is left handed circular polarized $|L\rangle$, and $|R\rangle$ is then the cross-polarized, right handed circular polarized field. t_x and t_y are the complex transmission coefficients for linear polarization directions orthogonal to the surface normal (along the coordinate x and y axes, respectively). Observing the transmitted field, it is clear

that the values of the phase function (1) are applied to the cross-polarized field $|R\rangle$ through the term $\exp(i\phi)$: I.e. the cross-polarized field will be focused to the focal point f , while the field remaining in the original polarization state is not. By appropriately designing the dielectric pillar periodicity p , height h , width w and length l one can tune t_x and t_y to increase the proportion of the transmitted field which is focused: By tuning the parameters such that $t_y = -t_x \equiv -t$ the metasurface also acts as a half-wave plate in which all the field is cross polarized, giving

$$|E_{\text{out}}\rangle = t \exp(i\phi)|R\rangle, \quad (4)$$

where now all the transmitted field is focused at the focal point. Since the phase $\phi(r)$ is imposed through the rotation (2) alone, the simulation task is limited to finding the dimensions p, h, w, l of the rectangular pillar array which optimize the degree of cross-polarization of the transmitted field. By fixing a common height h for all of the pillars, the metasurface can be flat and well suited for fabrication using lateral patterning techniques. Furthermore, as is common in literature (e.g [7,45].), we also apply the same values w and l to all rotated pillars and thereby disregard changes incurred upon t_x and t_y when rotating the rectangular pillars by the angle α . This simplification allows us to use a continuous range of angles $\alpha \in [0, \pi)$ and using identical (although rotated) pillars yields a constant filling factor over the UV-Nanoimprint Lithography stamp, which is an advantage towards process optimization (Sec. 3.1). Preliminary simulations for the Si rectangular pillars on a quartz substrate indicate that the phase discrepancies incurred by this simplification are at most (varying by angle α) on the order of around 0.03 rad. The transmittance discrepancies due to rotation seem to be negligible, however.

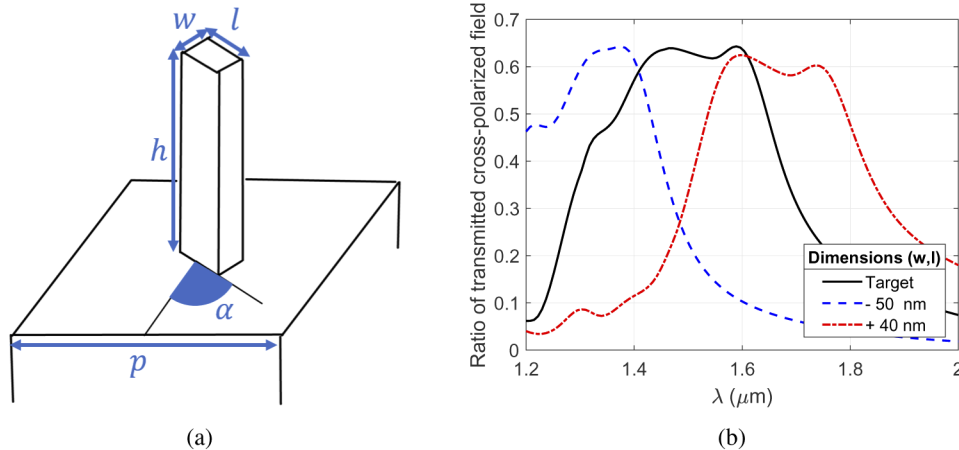


Fig. 1. (a) Sketch of Si rectangular pillars rotated by an angle α relative to the unit cell axes. When the incident field is circularly polarized, the rotation angle imposes a phase shift of 2α to the transmitted cross-polarized field. (b) Simulated cross-polarized intensity for left-circular field passing through an array of the sketched pillars using the Rigorously Coupled Wave Analysis (RCWA) method. The target dimensions of $h = 1200$ nm, width $w = 230$ nm, length $l = 354$ nm and periodicity $p = 835$ nm give the solid curve. Simulations for structures with reduced or increased lateral dimensions (by -50 nm and $+40$ nm) are displayed: These demonstrate that fabrication tolerances of at least ± 40 nm in the lateral dimensions should give functioning metasurfaces at either of two common telecom wavelengths $\lambda = 1.55 \mu\text{m}$ or $\lambda = 1.31 \mu\text{m}$.

2.2. Sweep simulations to find array dimensions

We performed sweep simulations to find array dimensions that maximize transmission of the cross polarized field using Rigorously Coupled Wave Analysis (RCWA) in the GD-Calc implementation

and the Finite Difference Time Domain method (FDTD) in the OptiFDTD implementation. We verified that the configuration of the two simulation methods were sound by demanding convergence between them. To this end it was found that above 12 diffraction orders gave sufficient convergence in the RCWA simulations. For the FDTD method, suitable values for the source pulse width (FWHM of $6.84 \cdot 10^{-15}$ s for the target wavelength $\lambda = 1.55 \mu\text{m}$), simulation time (25000 timesteps of $\Delta t = 5.5 \cdot 10^{-18}$ s) and mesh grid (discussed below) were determined. We used periodic boundary conditions around the unit cells (orthogonal to the optical axis) and perfectly matched layers at the beginning and the end of the optical axis. We find that dimensions of $h = 1200$ nm, width $w = 230$ nm, length $l = 354$ nm and periodicity $p = 835$ nm give full cross-polarization for the target wavelength of $\lambda = 1.55 \mu\text{m}$. For the FDTD method a non-uniform mesh grid was used to allow for a fine mesh near to the Si pillars, which is necessary for the simulation of washboard type sidewall surface roughness characteristic of the Bosch process (more about this in Sec. 2.3). For the directions orthogonal to the pillar heights (i.e. orthogonal to the optical axis) the FDTD mesh grid interspacings varied between $3 \text{ nm} \leq (\Delta x, \Delta y) \leq 6 \text{ nm}$, while along the optical axis the mesh grid interspacings varied between $3 \text{ nm} \leq \Delta z \leq 10 \text{ nm}$. The simulations assume the source is placed within the silicon (Si) substrate: I.e. reflections at the wafer backside are neglected because they can be effectively eliminated by use of an anti-reflection coating, and are not intrinsic to the metasurface design. The ratio of transmitted cross-polarization intensity to the intensity of the light incident on the metasurface is shown in Fig. 1(b). The lower than unity ratio may be largely attributed to reflections at the boundary between the Si substrate ($n_{\text{Si}} = 3.5$) and air ($n_{\text{air}} = 1$): The Fresnel equations at normal incidence give roughly 31% reflectance at a Si-air interface for the relevant wavelength bandwidth. The efficiency of the metalens can be increased by e.g. placing the Si metasurface pillars on a quartz substrate ($n_{\text{SiO}_2} = 1.5$) instead, which would reduce the corresponding reflectance to around 4%. The structures on the interface may of course also contribute to reduce the expected efficiencies somewhat: Some scattering to diffraction orders within the Si substrate is expected since $\lambda/n_{\text{Si}}p = 0.53$ for $\lambda = 1.55 \mu\text{m}$.

Development of a UV-NIL and Bosch DRIE patterning process for metalens fabrication involves many parameters that must be taken into account when aiming to end up with the desired lateral dimensions found from simulations. As such it is useful to know what tolerances are permitted in the lateral dimensions of the structure, when planning for the fabrication. Figure 1(b) shows two additional simulations where the lateral dimensions w and l of the pillars are varied to determine the permitted lateral fabrication tolerances. Increasing the lateral dimensions by 40 nm shows that the metasurface continues to have a high cross-polarization transmission at $\lambda = 1.55 \mu\text{m}$. While reducing the lateral dimensions by -50 nm gives low cross-polarization transmission at $\lambda = 1.55 \mu\text{m}$, a high transmission is achieved at another common telecom wavelength of $\lambda = 1.31 \mu\text{m}$. Therefore, when given the freedom of using either $\lambda = 1.55 \mu\text{m}$ or $\lambda = 1.31 \mu\text{m}$, the fabrication tolerance in the lateral dimensions is expected to be on the order of $\pm 40 \text{ nm}$. It is important to note that discrepancies in the lateral dimensions primarily affect the *efficiency* of the lens and *not* the focal spot size owing to the geometric phase effect (phase is imposed by rotation of the structure rather than its particular dimensions). This explains why our lenses fabricated in Sec. 3 attain diffracton-limited focusing despite slightly missing the target dimensions. Since high precision in reaching the target dimensions will be challenging under process development we have designed three designs to account for scenarios in which we might over- and under-estimate the end result dimensions. The variants of dimensions used for the fabrication of the NIL master are outlined in Table 1 in Sec. 3.

It turned out that the smallest variant (i.e. variant B) of the table was the best suited due to broadening at the base of the resist pillars (as discussed in Sec. 3.1).

2.3. Compensation for Bosch sidewall surface roughness

The center picture in Fig. 2(b) shows a SEM image of a Si rectangular pillar fabricated after Bosch-type 3-steps Deep Reactive Ion Etching (DRIE). As can be seen, the alternation of isotropic etching, passivation and de-passivation in the Bosch process leads to washboard surface patterns in the form of "scallops". In the research field it is sometimes pointed out that surface roughness poses a problem towards achieving high optical quality [7], however since the roughness in this case is regular and occurs on length scales that are much smaller than the wavelength we will now show that one can treat them (somewhat simplistically) as giving rise to effectively reduced pillar dimensions which can be compensated for by increasing the lateral dimensions of the pillars in the mask. To demonstrate this, consider the simple structure mimicking a Bosch processed pillar displayed on the right hand side of Fig. 2(b). In order to avoid complicated geometries, we have assumed half-cylindrical scallops characterized by a scallop radius R (in reality scallops are typically more elliptically shaped, as seen in Fig. 5(b) of Sec. 3.2, for which it is more appropriate to speak of scallop depths). In order to show that even medium to large scallops can be effectively compensated for, we choose a scallop radius of $R = 50$ nm, which is large relative to the lateral dimensions $w = 230$ nm and $l = 354$ nm of the smooth walled pillar displayed to the left of Fig. 2(b) (but still small compared to the design wavelength $\lambda = 1550$ nm). The scallop indents remove volume from the Si pillars by an amount corresponding to the half-cylinder volumes. To compensate for this volume loss we increase the lateral dimensions of the pillars. We can make a rough estimate to the needed increase based on keeping the volume filling factor of Si in the unit cell constant: The volume filling factor is left unchanged by the half-cylindrical scallops when the lateral dimensions are increased according to

$$w_c = w + \frac{\pi R}{2} = 308.5 \text{ nm},$$

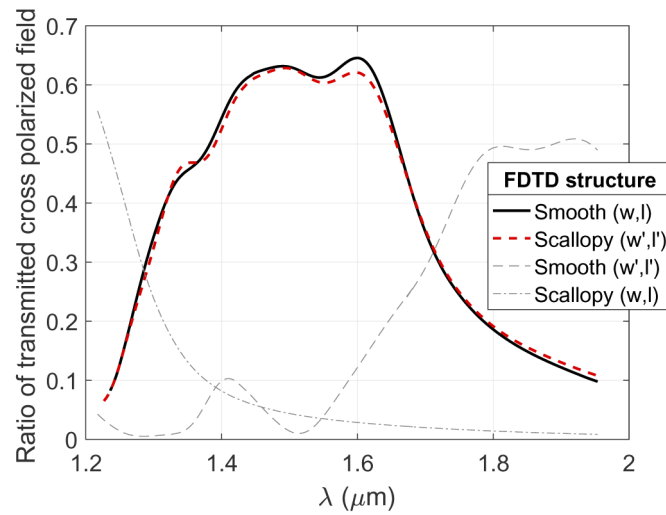
$$l_c = l + \frac{\pi R}{2} = 432.5 \text{ nm},$$

For very long wavelengths relative to the unit cell periodicity, where the volume filling factor tends to be more important than the geometry of the subunit structure, this compensation ought to work well. However, in our case where the design wavelength is only roughly twice the unit cell periodicity, this simple estimate will likely only approximately work as intended and may need refining. By simulating the pillar of dimensions w_c and l_c with half-cylinder scallops of radius R we end up with a cross-polarization intensity curve which is slightly blue-shifted relative to that of the smooth pillar: The peak intensity is $\lambda_c = 1.544 \mu\text{m}$ while the peak intensity of the smooth pillar is $\lambda_s = 1.603 \mu\text{m}$. In order to align the curves we therefore refine our estimate of the needed dimensions by scaling with the ratio of the peak wavelengths $\lambda_s/\lambda_c = 1.0382$. We therefore end up with a correction that is $\sim 3.82\%$ larger than that required to compensate for the direct volume loss due to the scallops:

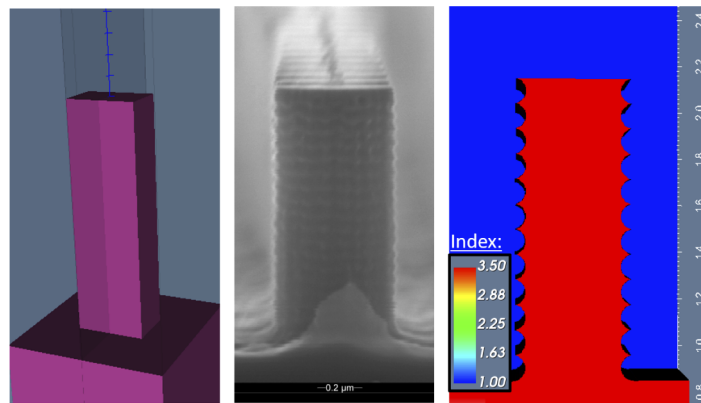
$$w' = 1.0382 \left(w + \frac{\pi R}{2} \right) = 320 \text{ nm}, \quad (5)$$

$$l' = 1.0382 \left(l + \frac{\pi R}{2} \right) = 449 \text{ nm}, \quad (6)$$

Note that the scaling factor 1.0382 is expected to change upon design: Following the reasoning above, we expect it for instance to depend on the periodicity to wavelength ratio, tending to unity as the ratio becomes small. The simulation result of using (5) and (6) is shown in Fig. 2(a) where the simulation labeled *Scallopy* (w', l') shows that essentially the same transmitted cross-polarization intensity curve is achieved for the scallopy structure as for the smooth-walled pillar (the simulation labeled *Smooth* (w, l)). For completeness, we have added two additional simulations to Fig. 2(a):



(a)



(b)

Fig. 2. (a) Simulated cross-polarized intensity for left-circular field passing through metasurfaces consisting of rectangular silicon pillars ($n = 3.5$) using the Finite Element Time Domain (FDTD) method. The curves labeled *Smooth* (w,l) and *Scallopy* (w',l') correspond to the two pillar illustrations in (b): The first being a pillar with smooth sidewalls, while the latter being a pillar with washboard sidewall roughness (i.e. mimicking the "scallop" sidewalls which can result from a Bosch DRIE process) where the lateral dimensions of the rectangular pillar have been increased to compensate for the volume loss caused by the scallops. The two curves give qualitatively equal cross polarization. For comparison, the curves *Scallopy* (w,l) shows the effect of adding the same scallops *without* increasing the lateral dimensions, while the curve *Smooth* (w',r') shows the effect of increasing the lateral dimensions without imposing scallops. (b) *Left*: The structure with smooth sidewalls for the FDTD simulations, with height $h = 1200$ nm, width $w = 230$ nm, length $l = 354$ nm and periodicity $p = 835$ nm. *Center*: A SEM image of a rectangular pillar etched into Si using Bosch DRIE. *Right*: Showing the refractive index cross-sectional profile of the FDTD simulation structure for an imitation of a rectangular Si pillar with "scallop" sidewalls (scallop radii of $R = 50$ nm) where the lateral dimensions have been scaled up to $w' = 320$ nm and $l' = 449$ nm in order to compensate for the volume loss by the scallops.

Scallopy (w, l) shows the effect of adding scallops ($R = 50$ nm) *without* adding to the lateral dimensions, while *Smooth* (w', r') shows the effect of adding to the lateral dimensions according to (5) and (6) without imposing scallops. Addition or removal of the scallops is therefore seen to shift the cross-polarization curves down and up in wavelength, respectively, which is in line with our proposal to interpret scallopy sidewalls as an effective reduction in lateral dimensions.

3. Results

This section describes the results of the UV-nanoimprint lithography (UV-NIL) and etching steps, as well as some of the challenges encountered. Proposed strategies towards process optimization are discussed in Sec. 4.

3.1. Imprint results

UV-NIL was done using the Micro Resist Technology mrNIL-210 series resist and a soft stamp (Solvay Fomblin MD-40). The stamp is an inverted copy of a silicon master wafer with nominally 500 nm tall pillars forming the metasurface (see Fig. 3(a)). In order to transfer this pattern to the silicon process wafers two conditions must be fulfilled: 1) the resist needs to be thick enough to function as an etch mask for more than 1.2 μm silicon DRIE, and 2) the residual layer thickness (RLT) of the remaining resist between the wafer surface and the imprinted pattern must be minimized (see Fig. 3(b)). In order to completely fill the inverted metasurface-structures in the stamp with resist, only a thin initial resist layer of less than 100 nm was needed for our design. However, in some cases it could be beneficial to have a thicker resist layer outside the patterned area, in order to prevent this area from being etched. Thus, resist films of different initial thicknesses from 500 nm and thinner were explored. The mrNIL210-200nm formulation, spun at 3000 rpm, gave low enough RLT values and acceptable variation over the metasurface. The resist thickness before imprint was measured by ellipsometry to be approximately 150 nm. The RLT obtained after imprint varied between $48\text{nm} \leq \text{RLT} \leq 74$ nm over the metasurface. While these RLT values were acceptable for further processing, the results obtained from the thicker mr-NIL210-500nm formulation were not viable for the metasurface patterning by DRIE: The RLT varied considerably over the lens, being at most always close to the pre-imprint resist film thickness. This finding turned out to be crucial for the ensuing fabrication.

In general metasurfaces consist of structures of varying geometry, which means that the filling factor F varies over the surface. Optimizing the RLT therefore becomes challenging, as the amount of resist used to fill the structures varies over metasurface. In this respect, our optical design based on the geometric phase method (Sec. 2.1) has the advantage of providing identical structures (although rotated) with identical filling factors over the metasurface. This makes process optimization of the residual layer thickness easier. As a side remark: We also attempted fabrication of another optical design based on cylinders of varying radii in which issues with delamination of resist upon stamp removal seemed to depend on filling factor of the cylinders (see Fig. 4).

An issue with the imprinted structures is broadening close to the base of the resist pillars (a resist "foot") as seen in Fig. 3(c). Such broadening is also frequently observed in SEM images from literature [47–49]. This resist foot leads to an added length in the lateral dimensions of the rectangular pillars, which is transferred to the final pillar dimensions in the patterned silicon (Sec. 3.2). We believe this broadening effect likely originates from the master wafer (from which the soft stamp is made) since the UV-cured resist generally follows the pattern of the master. Section 3.2 outlines how we resolved the issue by means of various etch parameters for the resist pillars.

Attaining sufficient adhesion between the resist and the substrate remains an important issue. This is necessary to avoid delamination of the metastructure when the stamp is withdrawn from the surface after exposure. Such adhesion issues are unwanted if NIL is to become

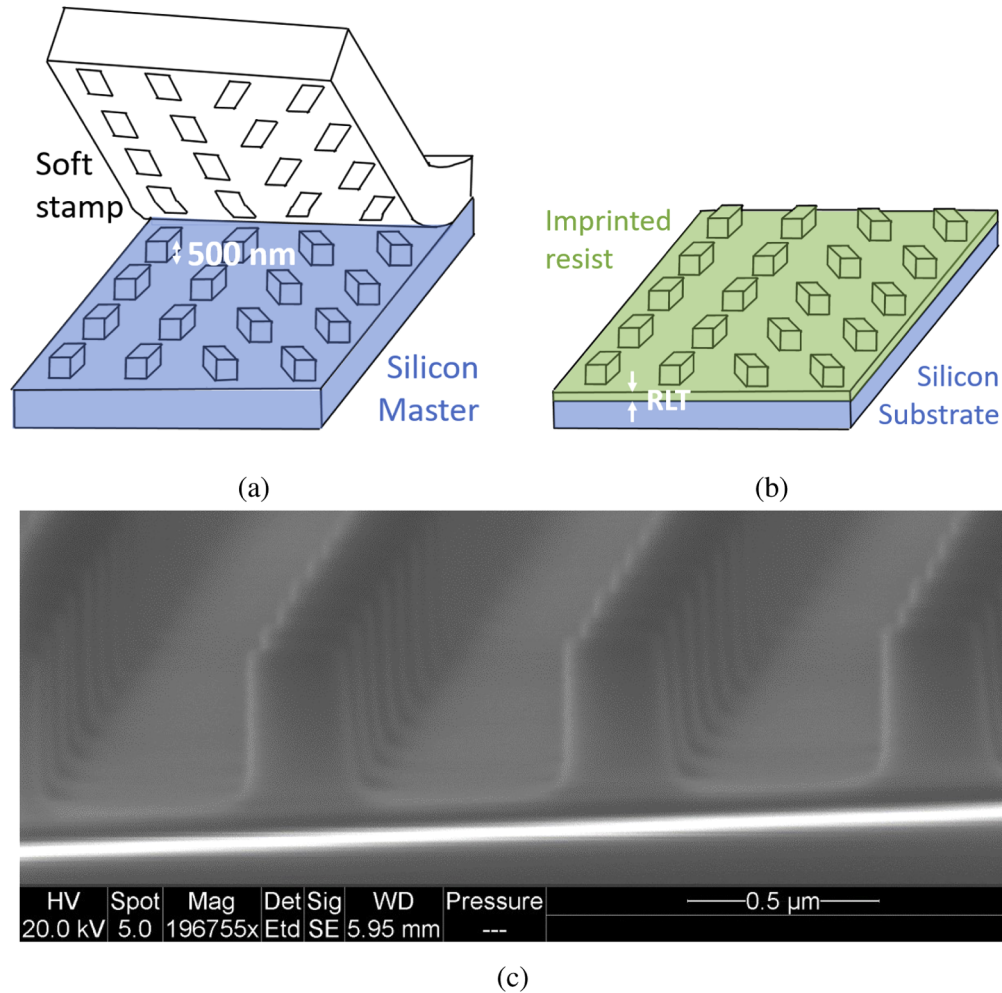


Fig. 3. (a) *Sketch of stamp fabrication:* A soft stamp is made by spinning Solvay Fomblin MD-40 onto a Si master wafer covered with nominally 500nm tall rectangular pillars, rolling on a carrier foil, exposure by UV illumination and finally detaching the stamp. The stamp is therefore an inverted copy of the silicon master, consisting of rectangular holes which are nominally 500nm deep. (b) *Sketch of resist mask after imprint:* The soft stamp has been rolled onto a film of Micro Resist Technology mr-NIL210 series resist covering a bulk Si wafer substrate primed with mr-APS1. After exposure to UV illumination, the stamp is removed. What remains is patterned resist (a copy of the original master). Between the patterned resist and the silicon substrate there exists a film of residual resist characterized by a Residual Layer Thickness (RLT). (c) *Cross-sectional SEM image of imprinted and exposed resist on a silicon substrate:* The bright white line is probably caused by delaminated resist at the edge. Between the resist pillars and the silicon substrate one can observe the RLT. One also observes a broadening at the base of the resist pillar (in the shape of a "top-hat").

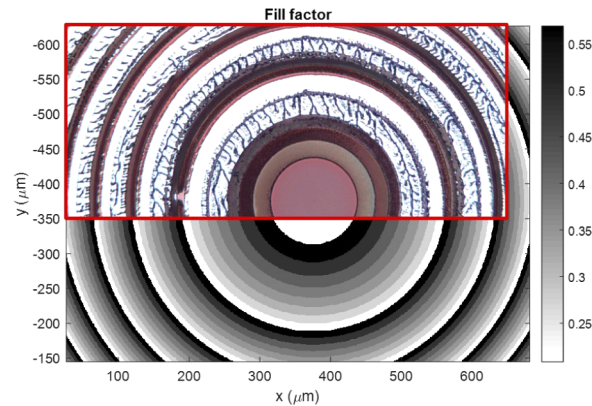


Fig. 4. Imprint challenges when filling factor varies over metasurface. Here a cropped microscope image of imprinted resist (red border) is placed on top of the plotted fill factor (gray scale plot) of a metalens consisting of cylindrical pillars of varying radii. As can be seen, the structural fidelity of the imprint varies dramatically with filling factor (F): Areas with large F seem to turn out well, whereas areas with low F seem to detach with the stamp (apart from the center area).

a high-throughput metasurface fabrication technique. To facilitate adhesion, RCA cleaned substrates were plasma activated (600W for 10mins) before spinning adhesion promoter (mr-APS1) immediately afterwards. Three different dimensions of resist pillars corresponding to filling factors $F_1 = 0.12$, $F_2 = 0.17$, $F_3 = 0.24$, respectively, were used for the metastructure (corresponding to the dimensions in Table 1). However only the smallest gave reliable imprinting. The imprints with larger filling factors more or less consistently delaminated when withdrawing the stamp after exposure.

Table 1. Lateral dimensions and filling factors of rectangular pillars for mask fabrication

| Metasurface | w [nm] | l [nm] | Filling factor (F) |
|-------------|----------|----------|------------------------|
| A | 292 | 416 | 0.17 |
| B | 237 | 361 | 0.12 |
| C | 351 | 475 | 0.24 |

3.2. Etch methodology and results

In order to transfer the imprint patterns (as shown in Fig. 3(c)) to the silicon wafer we utilized first a continuous (un-pulsed) RIE step to etch through the residual layer of resist before commencing with Bosch 3-step DRIE - i.e. pulsed etching consisting of the three steps passivation, de-passivation and isotropic SF_6 -based silicon etch. Figure 5(a) shows that high pattern fidelity is achieved in the silicon: We observe vertical sidewalls (indented with scallops, discussed below) for the pillars of around $1.2 \mu\text{m}$ height. In a separate run we observed the same pattern fidelity to at least $1.6 \mu\text{m}$ etch depth. The cyclically-pulsed etching of the Bosch process leaves a washboard-like surface roughness characterized by a scallop depth which depends on the parameters of the Bosch process. For Fig. 5(a) the scallop depths are $\sim 14 \text{ nm}$. In making these structures we used 6" Si bulk wafers on which only a small area was patterned: 4 metalenses (rectangular pillars) of area $1.5\text{mm} \times 1.5 \text{ mm}$, and one metalens (cylindrical pillars) of $0.75\text{mm} \times 0.75\text{mm}$. During the first RIE dry-etch step (for residue layer removal) the resist is completely

removed from the surrounding wafer surface, resulting in an etch loading close to 100% for the following Bosch DRIE step (to etch the Si pillars).

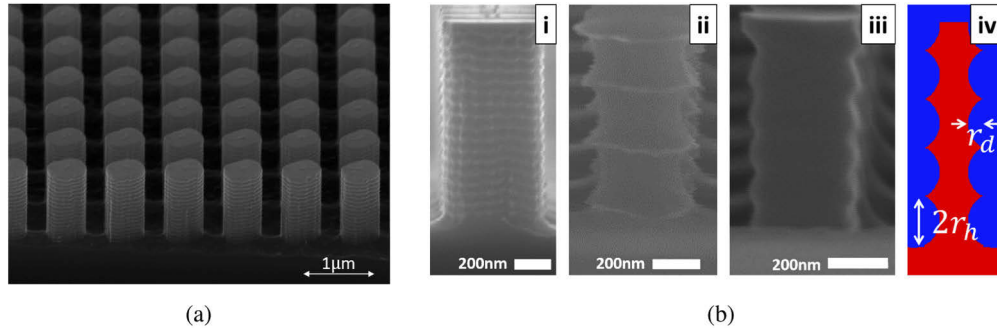


Fig. 5. (a) Patterned silicon after Bosch Deep Reactive Ion Etching (DRIE) of the silicon wafer with imprinted resist as pictured in Fig. 3(c). The pulsed etching of the three-step Bosch process leads to washboard sidewall surface roughness. (b) Three different scallop depths achieved using DRIE: (i) A close-up of the metasurface pictured in (a) with scallop depths of around ~ 14 nm, (ii) In order to reduce the effective dimensions of the pillars, closer to the target dimensions, the scallop depths were increased to ~ 76.5 nm. The scallop heights are measured to be ~ 119 nm (taking into account a 10° viewing angle). Note that the resist has not been stripped in this image (although the resist is not clearly seen in the image). (iii) Dimensions close to the target were achieved by first performing a Bosch DRIE leading to scallops of depths ~ 44 nm, thereafter performing an oxidation step and oxide strip which in the end lead to scallop depths of ~ 29 nm. (iv) Shows how the scallop depth r_d and scallop height $2r_h$ is measured.

As discussed in Sec. 3.1, the broadening of the resist pillars seen in Fig. 3(c) leads to added dimensions in the etched structures. The pillars shown in Fig. 5(a) have lateral dimensions of around $420 \text{ nm} \times 530 \text{ nm}$, i.e. roughly 180 nm too large in both directions in comparison to the simulation designs in Sec. 2.2. As a result the optical properties of this metasurface lens are poor. To solve this issue without redesigning the mask, three approaches were tested. First we attempted an increased length of the continuous dry-etch step to attempt to completely remove the resist "foot" at the base of the imprinted resist pillars. Although this somewhat deteriorated the quality of the imprinted pattern (turning the resist pillars into pyramids), this did not seem detrimental to the patterning of the Si pillars. We expect that further development of the process parameters of the continuous dry-etch step will likely remove the unwanted broadening (as e.g. seen in [47] where the resist "feet" are removed completely while keeping vertical sidewalls in the resist), but the aforementioned run did not reduce it sufficiently. Our second approach was to dramatically increase the scallop depths to ~ 76.5 nm (see Fig. 5(b) ii) and the lateral dimensions were on the order of $307 \text{ nm} \times 460 \text{ nm}$ (measured between the tops of the washboard pattern). A third approach consisted in realizing less extreme scallop depths of ~ 44 nm and thereafter oxidizing the structures so that around 100 nm oxide resulted. After stripping this oxide away (which on a planar silicon surface would have resulted in 44 nm reduced silicon thickness on each surface) the scallop depths were reduced to around ~ 29 nm (see Fig 5(b) iii) and the lateral dimensions were on the order of $210 \text{ nm} \times 320 \text{ nm}$.

3.3. Optical characterization

The two metalenses from the fabrication steps discussed in Sec. 3.2 were tested optically using the measurement setup shown in Fig. 6. One of the metalenses had comparatively large scallop depths of ~ 76.5 nm and lateral dimensions on the order of $307 \text{ nm} \times 460 \text{ nm}$ as shown in

Fig. 5(b) (ii) (hereafter called MLII). The other metalens had shallower scallops of ~ 29 nm and lateral dimensions on the order of $210 \text{ nm} \times 320 \text{ nm}$, shown in Fig. 5(b) (iii) (hereafter referred to as MLIII). Note that while the metasurfaces were designed for left circular polarization, the transfer of the pattern to the nanoimprint master led to opposite rotation of cylinders compared to the simulations and consequently a change in the handedness of the circular polarized light for operation. Hence for the optical characterization, the metasurfaces are illuminated with right handed circular polarized light, and the metasurfaces focus the cross-polarized left handed circular polarized light.

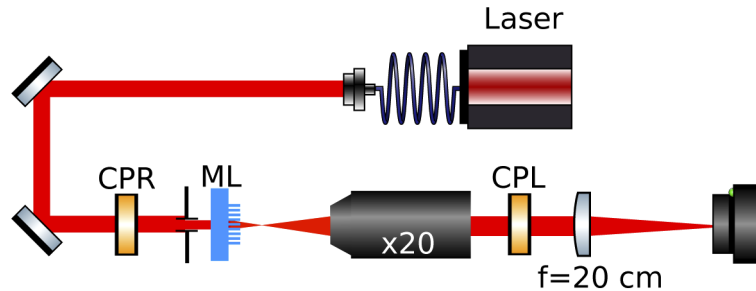


Fig. 6. Optical setup used to characterize the metalenses. A collimated laser beam passes through a right handed circular polarizer (CPR), before going through an aperture with diameter 0.9 mm and then the metalens (ML). The beam is converted to left handed circularly polarized light and focused by the metalens. The resulting focal spot is imaged onto an IR camera using a x20 infinity corrected microscope objective and a planoconvex lens. A left handed circular polarizer (CPL) is placed in reverse between the microscope objective and the planoconvex lens, such that only the light which is converted from right to left handed circular polarization by the metalens is let through. When measuring the focal spot for the aspherical lens, the right handed circular polarizer is moved in front of one of the alignment mirrors, such that the handedness is changed by the mirror and the light can pass through the left handed circular polarizer. The aperture is used to ensure the lenses have the same effective numerical aperture, and a powermeter is used to ensure the same amount of light is transmitted through the aperture for all measurements.

The focal spots of the metasurfaces are shown in Fig. 7 for two wavelengths, $1.31 \mu\text{m}$ and $1.55 \mu\text{m}$, together with the focal spot of an anti-reflection coated aspherical lens with a focal length (10 mm) and the same aperture (0.9 mm diameter) for comparison. The metalenses are designed to have the same focal length of 10 mm at the target wavelength of $\lambda = 1.55 \mu\text{m}$, and we measure the focal spots to lie around 10.2 mm in the case of MLII and 10.1 mm in the case of MLIII. Both metalenses give spot sizes which match the aspherical lens and the theoretical diffraction limit. For the measurement at $\lambda = 1.31 \mu\text{m}$ the focal lengths of the metalenses increase to around 12 mm due to large chromatic aberrations (a characteristic trait of dielectric pillar metalenses [7,8]), while the focal length of the aspherical lens is increased to 10.2 mm (i.e. its focal shift is an order of magnitude less). As a result, the diffraction patterns of the metalenses at $\lambda = 1.31 \mu\text{m}$ are slightly broader than that of the aspherical lens. The focal spots of the metalenses at $\lambda = 1.31 \mu\text{m}$ are nonetheless diffraction limited: They match the plotted theoretical diffraction pattern for a perfect lens of focal length of 12 mm. This is because little phase error over the lens is incurred upon shifting from the design wavelength $\lambda = 1.55 \mu\text{m}$ to $\lambda = 1.31 \mu\text{m}$ due to the focal lengths of the metalenses being roughly ten times larger than their size. For incident light that has left handed circular polarization, the metalenses are divergent, having a focal length at $\lambda = 1.55 \mu\text{m}$ of around -10 mm. This was confirmed by switching the polarizers and observing the virtual focal spot visible when bringing the metalens around 10 mm inside the working distance of the microscope objective.

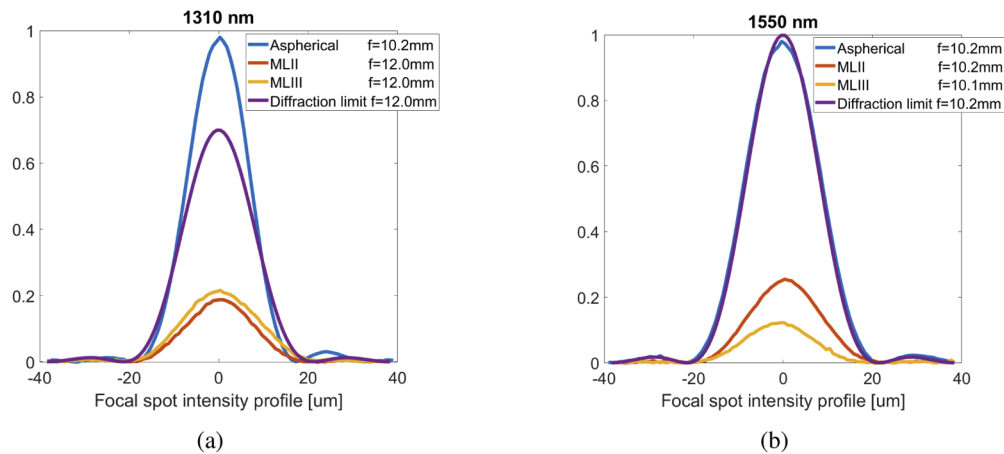


Fig. 7. Focal spot profiles measured for two metalenses and an anti-reflection coated aspherical lens when focusing a fully polarized and collimated laser beam of wavelength 1310 nm (a) and 1550 nm (b). For all lenses and for both wavelengths an aperture with diameter 0.9 mm has been placed in front of the lens.

At $\lambda = 1.55\mu\text{m}$ MLII has a measured efficiency of 25.5% and MLIII has a measured efficiency of 12.2%. The measurements were made by comparing the peak values in Fig. 7, and by disregarding reflection at the substrate back-side (by dividing the measured intensity by 0.69). When estimating the efficiency at $\lambda = 1.31\mu\text{m}$, the aforementioned focal spot broadening for the metalenses means that the peak intensity ratio to that of the aspherical lens underestimates the power efficiencies (the ratio of area under their curves is larger than the ratio of their peak intensities). So although the measured relative peak intensity at $\lambda = 1.31\mu\text{m}$ is 18.7% for MLII and 21.6% for MLIII, the actual power efficiency is 25.4% for MLII and 29.2% for MLIII. These efficiency values are found by dividing by a correction factor of 0.74 which is found from the

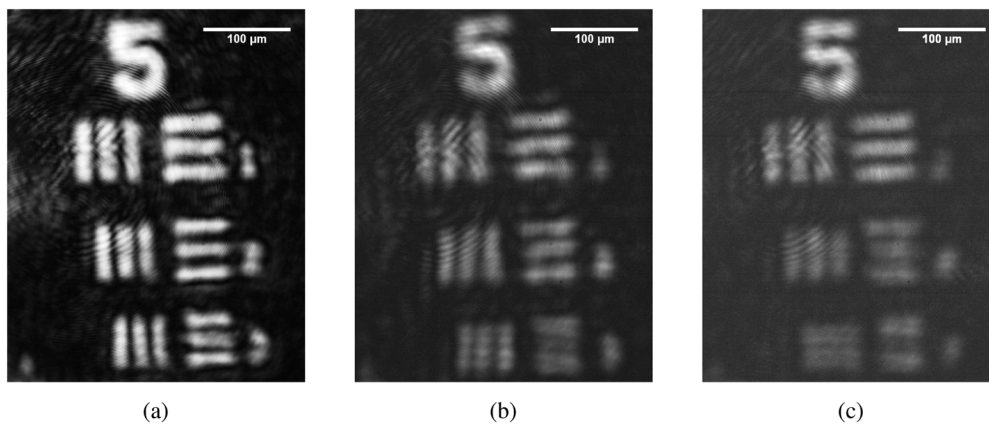


Fig. 8. Images of a resolution target using an aspherical lens (a), metalens MLII (b), and metalens MLIII (c). The groups of lines have widths $15.6\mu\text{m}$, $13.9\mu\text{m}$ and $12.4\mu\text{m}$. The target is illuminated by a 1550 nm laser beam, and to enable comparison of the lenses an aperture with diameter 0.9 mm has been placed in front of the lens. The contrast is significantly better for the aspherical lens, while the resolution is only slightly better - the $13.9\mu\text{m}$ thick lines in (b) are resolved similarly to the $12.4\mu\text{m}$ thick lines in (a).

ratio of peak intensities of ideal diffraction patterns for lenses with the two focal lengths of 10mm and 12mm. Note that the beam quality of the diode laser used for the $\lambda = 1.31 \mu\text{m}$ measurement is significantly lower than that of the fiber-laser used for the $\lambda = 1.55 \mu\text{m}$ measurement, adding some uncertainty to this measurement.

Both of the measured lens intensities at the target wavelength $\lambda = 1.55 \mu\text{m}$ are less than half of the simulated cross polarization efficiency of the target design (Fig. 2). It should be noted that the simulations do not consider a lens, but rather an infinite array of identical structures. There are a number of loss mechanisms that apply when the array of structures are rotated to match the phase equation of a lens (1) (as discussed in Sec. 2.1), for instance diffraction loss. That being said, we expect the most significant cause for the low efficiency is due to discrepancy between the effective lateral dimensions of the fabricated structure and the target dimensions. As discussed in Sec. 2.1 for metalenses based on the geometric phase principle, discrepancies in the lateral dimensions do not primarily affect the focal spot size, but rather affect the lens efficiency. It therefore seems plausible that the approaches we have used to reduce the effective

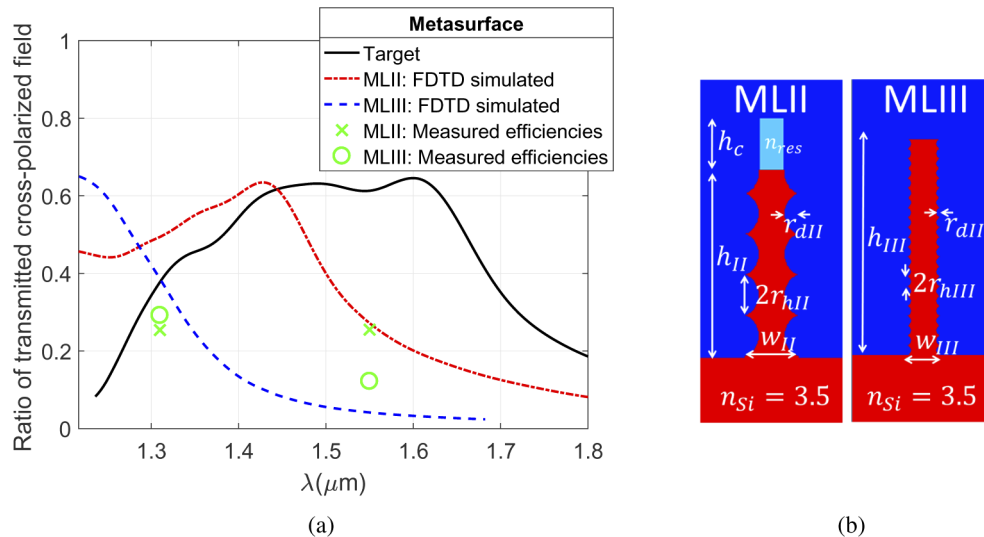


Fig. 9. (a) Simulations on structures that mimic those seen in the SEM images of the fabricated structures in metalenses MLII and MLIII (Fig. 5(b)). The target curve for a smooth pillar (shown earlier in Fig. 2(a)) and the measured efficiencies of the fabricated lenses are added for comparison. It is seen that the strategy of using large scallops (MLII) and smaller scallops + oxidation + oxide strip (MLIII) to reduce the pillar dimensions, as discussed in Sect 3.2, result in curves that are shifted to lower wavelengths relative to the target. (b) Refractive index cross-sectional profile of structures that mimic the fabricated structures in MLII and MLIII. Parameter values for the MLII mimic: $w_{II} = 307 \text{ nm}$, $l_{II} = 406 \text{ nm}$, $r_{hII} = 119 \text{ nm}$, $r_{dII} = 76.5 \text{ nm}$, $h_{II} = 1100 \text{ nm}$, $h_c = 300 \text{ nm}$ and $n_{res} = 1.44$. Parameter values for the MLIII mimic: $w_{III} = 210 \text{ nm}$, $l_{III} = 320 \text{ nm}$, $r_{hIII} = r_{dIII} = 29 \text{ nm}$, and $h_{III} = 1270 \text{ nm}$. To best mimic the structure of MLII (which has very large scallops, as seen in Fig. 5(b)), we have drawn a structure with elliptical scallops characterized by both a scallop depth r_d and a scallop height r_h . At the top of these pillars we have also placed a 300 nm thick capping layer of lower refractive index $n_{res} = 1.44$ to account for some resist that remained despite our efforts to remove after dicing the chips. Simulations however show that this capping layer makes insignificant changes to the cross-polarization curve between $1.31 \mu\text{m} \leq \lambda \leq 1.55 \mu\text{m}$. For MLIII we were able to remove the resist prior to dicing the metasurface lenses thanks to access to a plasma stripper tool for whole wafers.

pillar dimensions (described in Sec. 3.2) may have reduced them slightly too much: This is also the impression from viewing the SEM images in Fig. 5(b). To investigate this hypothesis Fig. 9 shows simulations for structures which mimic the fabricated structures in MLII and MLIII, together with the simulation of the target structure (i.e. the smooth wall pillar simulated in Fig. 2(a)). The chosen parameters for the simulation are listed in the caption of the figure. Although attempting to simulate the fabricated structures involves some approximation and is prone to some uncertainty (using simpler geometries and relying on local and uncertain SEM measurements), we find a good qualitative match with our hypothesis that the scallops have reduced the pillar dimensions slightly too much: In Fig. 9 the cross-polarization curves for the MLII and MLIII mimicked structures are seen to be shifted to lower wavelengths than the target curve, clearly resulting in a lowering of the lens efficiency at the target wavelength $\lambda = 1.55 \mu\text{m}$. Furthermore, since the curve of MLIII is shifted further away from the target than MLII, it also attains a lower efficiency than MLII at $\lambda = 1.55 \mu\text{m}$. We have also plotted the measured lens efficiencies at $\lambda = 1.31 \mu\text{m}$ and $\lambda = 1.55 \mu\text{m}$ for comparison, although with so few data points (and the aforementioned uncertainties in simulations and measurement) it is hard to draw any conclusions about the shifting of the curves from these.

The same measurement setup was also used to take images of a resolution target using the metalenses. For these measurements the resolution target was placed 2 cm in front of the metalens, and the image plane 2 cm behind the metalens was imaged onto the camera using the microscope objective and planoconvex lens. Figure 8 shows the resulting images for the two metalenses and the aspherical lens using the 1550 nm laser. The aspherical lens has clearly better contrast owing to higher efficiency, while the resolution is only slightly better for the aspherical lens, since $13.9 \mu\text{m}$ thick lines are resolved similarly by the metalens as $12.4 \mu\text{m}$ thick lines are resolved by the aspherical lens. Since all three lenses are observed to have the same diffraction limited focal spot size when the incoming light is collimated parallel to the optical axis, the slight difference in resolution when imaging the resolution target is likely due to coma [2].

4. Discussion

4.1. Towards process optimization

Our results have demonstrated the feasibility of using UV-NIL with subsequent continuous RIE and Bosch DRIE to fabricate diffraction limited metalenses. Further optimization towards high-throughput production relevant processing should aim at improving resist adhesion upon stamp detachment and a reduction of resist broadening at the base of the resist pillars in order to obtain greater precision in reaching the target dimensions (and thereby raising the efficiency of the lenses). This section discusses these challenges in turn.

A significant challenge in our UV-NIL patterning process was to avoid delamination of the resist upon detachment of the soft-stamp. To some extent, our experiences seems to indicate a degree of trade-off between achieving a low residual layer thickness (RLT) in the resist (Sec. 3.1) and its adhesion to the substrate. Despite the use of plasma-activation of cleaned substrates and quick subsequent application of an adhesion promoter (Sec. 3.1), the soft-stamp was in need of replacement typically after 3-5 imprints due to delamination of resist into the holes of the stamp (see Fig. 3(a) for sketch of the softstamp). This was in the case of the patterns of variant B in Table 1 which have the lowest filling factors $F = 0.12$. For the case of variants A and C (which have larger filling factors of $F = 0.17$ and $F = 0.24$), the resist patterns more or less consistently delaminated on the first imprint. However, the issues with delamination seemed only to occur after having switched to the less viscous resist formulation (mr-NIL210-200nm) for which the desired low residual layer thickness (RLT) resist values were attained. While using the more viscous resist formulation (mr-NIL210-500nm) the imprint patterns of all filling factors more or less consistently turned out well. Unfortunately, as discussed in Sec. 3.1, the resulting RLT values of the more viscous resist formulation were too large for the subsequent etching steps. Further

process development of the UV-NIL patterning steps should therefore consider varying the RLT further by dilution of mr-NIL210-500nm and see if there exists a lower threshold of the RLT at which the adhesion issue ceases. The silicon pillars in our master wafer had slightly angled sidewalls ($>80^\circ$) which are known to facilitate the release of the imprint stamp [50]. Another strategy could be to test even larger angles: Tuning the etch properties of the master fabrication may allow for controllable sidewall angles, and for a systematic analysis of these with respect to soft stamp release. Although slight sidewall angles may be beneficial in this respect, the transfer of such sidewalls to the resist pillars in the mask may add uncertainty for reaching the desired lateral target dimensions.

The occurrence of broadening at the base of the resist pillars (like "top-hats", see Fig. 3(c)) lead to a broadening of the etched Si pillars in comparison to the mask dimensions of variant B in Table 1 (becoming roughly 180 nm too large). While we demonstrated that this could be compensated for by both increasing the lateral etch depth (i.e. scallop depths) of the Bosch pulsed DRIE (shown in Fig. 5(b)(ii)) and through oxidizing and stripping (shown in Fig. 5(b)(iii)) as discussed in Sec. 3.2, the addition of these processing steps also add uncertainties in predicting the resulting dimensions of the Si pillars: As was noted in Secs. 3.2 and 3.3, the resulting effective dimensions of the Si pillars with large scallop depths became slightly too small in comparison to the target values, which in turn may explain why the lens efficiencies are lower than their theoretical limits. Similar resist broadening to what we have observed seems to be commonly encountered in literature [47–49]. The authors of [47] demonstrate that the unwanted broadening at the base of the resist pillars can be successfully removed along with the RLT layer by use of an O_2 plasma, leaving the resist pillars with almost vertical walls. However, achieving similar results for rotating rectangular pillars where the minimum distance between pillars vary over the lens will likely require significant process development.

Both strategies of processing away the issues of resist broadening in the imprinted resist discussed so far may require significant process development in order to reduce uncertainty in the resulting Si pillar dimensions. It would be preferable, therefore, to avoid the broadening in the first place: Avoiding the need to remove or correct for the resist "feet" at the base of the pillars, is expected to lead to better precision in reaching the target dimensions. This in turn should make it possible to develop more robust processes towards achieving diffraction limited metalenses of high efficiency. We believe the resist broadening likely originates from equivalent broadening being already present in master Si pillars and/or in the NIL stamp holes since the UV-cured resist generally follows the pattern of the stamp. It may be worth considering whether process development of the NIL master fabrication can lead to Si pillar patterns without curvature at the base.

4.2. Bosch process in comparison to competing etching techniques

The selection of the most appropriate plasma etch type for industrial metalens fabrication is not clear-cut. One group of process alternatives is a continuous reactive ion etch (RIE) - be it a classical parallel-plate RIE, or more advanced and better controlled inductively coupled plasma (ICP) based RIE, or a capacitively coupled plasma (CCP) RIE. The most advanced etchers are ICP-based. Another dry etch type is so-called cryogenic etch or cryo etch, which runs at temperatures lower than minus 100°C , also in a continuous fashion. The pulsed Bosch-type process (with two pulses, or the extended Bosch with three pulses, for each etch step) is the third of the main categories/candidates. Bosch deep reactive ion etch (DRIE) produces sidewalls that are not formally straight, but indented with "scallops", which is the main feature distinguishing Bosch from the others in terms of wall appearance. The "envelope" wall can be made very close to vertical, though, and the scallops could be made as small as 10 nm (depending on mask thickness and selectivity).

Cryo etch has experienced a certain popularity in R&D - in particular due to its smooth and mirror-like sidewalls and capability of high aspect ratio (HAR) etching. Cryo etch has, however, been little used by industry, owing to its rather serious drawbacks - all stemming from a very high demand on accurate temperature control of the wafer and its etched structures. This translates into a lack of process controllability, uniformity, and repeatability, as well as the need for a continuously running line for substrate/wafer cooling by liquid nitrogen. For HAR, Bosch as well as Cryo can go much further than non-cryo continuous RIE alternatives, and Bosch is the HAR dry etch process of choice in industry. Some recent indications exist that Cryo is gaining increased interest also in industry [51] due to its specific merits compared with Bosch. One merit of interest for this paper is the entirely smooth walls, which are preferable in masters for nanoimprint lithography. Even a wall angle slightly lower than 90 degrees is preferred, and easier made by cryo than Bosch.

For dielectric metalens and other meta-structures, published papers show requirements on etch aspect ratios (ARs) (i.e. gap AR, not pillar AR) ranging all the way from 2:1 to above 30:1 (see e.g. [1,3,7,8,34,35,52]). Furthermore, the minimum gaps between neighboring pillars range from less than 20 nm to several hundreds of nm. These widely differing ranges stem from a combination of the wavelength of the application, other parts of the specification, and the applied technology and materials. Roughly speaking, dry etched silicon metastructures operating in NIR tend towards lower AR ranges [3,52], whereas ALD deposited TiO₂ metastructures operating in VIS tend towards high aspect ratios (HAR) [7–9] (if they instead were to be made by etching). In terms of selecting the most appropriate etch type, one should (perhaps a bit simplistically) distinguish between low-to-medium range ARs, and a high aspect ratio (HAR) range. No strictly defined border exists between the two, and indeed it depends on several parameters and on one's final target, but a border could arguably lie very roughly at 10:1, or in some cases quite a bit higher. For low-to-medium gap ARs it is not always evident that a classical RIE or ICP-RIE (or CCP-RIE) must yield to a Bosch or a cryo etch, despite the latter two being clearly better than the others at HARs. Indeed, most papers in the field used ICP-RIE, and Ref. [1] achieves etching of ARs of 9:1 by ICP-RIE, and Ref. [35] ARs of about 7:1.

Still, continuous RIE could be more challenging than a Bosch or cryo process in obtaining straight (vertical) sidewalls (see e.g. [52]). Furthermore, a Bosch process stops more abruptly on a buried oxide layer (BOX), as provided by Silicon On Insulator (SOI) wafers, a convenient feature for precise height control. However, with the extremely small sideways dimensions in such metalens pillars (e.g., a pillar width of 55 nm in [52] and even 40 nm in the TiO₂ case of [7]), a very strict control of scallop size as well as sideways "notching" (a badly controlled sideways etch that can appear due to charging of the oxide) is required. The undesired notching effect could be mitigated by time-based stop of the Bosch DRIE just before the BOX is reached, followed by a well-tuned continuous RIE step. Another possible argument against the Bosch process is that it will always result in a pillar wall shape defined by scallops. However, as discussed in Secs. 2.3 and 3.3 this effect by itself does not seriously deteriorate metalens performance when it is corrected for in the NIL master - a key finding of our paper.

As noted above, it is possible that for some metalens designs the distance between neighboring pillars could become seriously small; thus, a limit exists for how long one can compensate for scallops by making the master pillars wider. However, as scallops at least under some circumstances could be made as small as 10 nm, very little master correction may often be required. A published example [7], though, shows gaps smaller than 20 nm. This not only gives an AR of over 30:1 in their design, but also strains the viability of scallop correction. In such an extreme situation, a cryo etch may be the best process option - if it is available.

In terms of access, Bosch process equipment is currently much more available than cryo, in R&D as well as industrial facilities. Almost all labs that do any serious silicon etching have Bosch processes at hand. However, the same basic plasma tool can be used for cryo as well as

Bosch, with relatively limited alterations to enable cryo. It is thus probably more likely that for a metalens development project a Bosch rather than a cryo process would be used in an R&D lab, while for an industrial enterprise one would think that comparative performance is the decisive factor.

All in all, there is in our opinion no clear and obvious "winner" in the etch type competition for metalenses. However, as long as the scallops of the Bosch-etched walls are not a serious hindrance performance-wise and do not lead to unfeasible narrow pillar cross-sections, and the pillar gaps are not extremely small combined with very high ARs, Bosch DRIE at the very least seems like a strong contender in many situations.

5. Conclusion

Diffraction limited dielectric metalenses have been fabricated using UV-Nano Imprint Lithography (UV-NIL) and a combination of continuous Reactive Ion Etching (RIE) and pulsed Bosch Deep Reactive Ion Etching (DRIE). These are standard silicon (Si) processing techniques that are relevant as the metasurface research field turns towards applications. In particular UV-NIL has been proposed as a strong candidate to replace the use of Electron Beam Lithography when seeking to achieve a high-throughput and large-area patterning technique. Simulations show that the "washboard-type" sidewall surface roughness characteristic of the Bosch DRIE process can be compensated for by increasing the lateral dimensions of Si pillars, and the fabricated structures have demonstrated diffraction-limited imaging despite the fact that its metastructure contains relatively large scallop depths. As such, the characteristic sidewall surface roughness of Bosch DRIE does not prevent the technique from being a strong candidate towards industrial metalens fabrication. It may however face some fundamental challenges in compensating for its sidewall roughness if seeking to fabricate nano-structures separated by high aspect ratio gaps.

The main challenges towards fabrication of the metalenses have been issues with delamination of the resist mask upon stamp removal and resist broadening at the base of the resist pillars. The latter lead to the lateral dimensions of the resulting Si pillars after etching being too large. These were compensated for by increasing the lateral etch depths in the pulsed Bosch Deep Reactive Ion Etching: I.e. the effective dimensions were reduced by increasing the scallop sizes. This resulted in diffraction limited lenses with measured efficiencies of 25.5% and 29.2% at wavelengths $\lambda = 1.55\mu\text{m}$ and $\lambda = 1.31\mu\text{m}$, respectively. Process optimization strategies are discussed to improve resist adhesion and resolve the issue of resist broadening. The latter strategies should lead to improved precision in reaching the desired Si pillar dimensions, which in turn is expected to raise the efficiency of the lenses.

Funding

EEA Grants 2014-2021 (Project contract no.5/2019).

Disclosures

The authors declare no conflicts of interest.

References

1. S. M. Kamali, E. Arbabi, A. Arbabi, Y. Horie, and A. Faraon, "Highly tunable elastic dielectric metasurface lenses," *Laser Photonics Rev.* **10**(6), 1002–1008 (2016).
2. A. Arbabi, E. Arbabi, S. M. Kamali, Y. Horie, S. Han, and A. Faraon, "Miniature optical planar camera based on a wide-angle metasurface doublet corrected for monochromatic aberrations," *Nat. Commun.* **7**(1), 13682 (2016).
3. E. Arbabi, J. Li, R. J. Hutchins, S. M. Kamali, A. Arbabi, Y. Horie, P. Van Dorpe, V. Gradinaru, D. A. Wagenaar, and A. Faraon, "Two-photon microscopy with a double-wavelength metasurface objective lens," *Nano Lett.* **18**(8), 4943–4948 (2018).
4. E. Arbabi, A. Arbabi, S. M. Kamali, Y. Horie, M. Faraji-Dana, and A. Faraon, "Mems-tunable dielectric metasurface lens," *Nat. Commun.* **9**(1), 812 (2018).

5. H. Pahlevaninezhad, M. Khorasaninejad, Y.-W. Huang, Z. Shi, L. P. Hariri, D. C. Adams, V. Ding, A. Zhu, C.-W. Qiu, F. Capasso, and M. J. Suter, "Nano-optic endoscope for high-resolution optical coherence tomography in vivo," *Nat. Photonics* **12**(9), 540–547 (2018).
6. R. C. Devlin, M. Khorasaninejad, W.-T. Chen, J. Oh, and F. Capasso, "High efficiency dielectric metasurfaces at visible wavelengths," arXiv preprint arXiv:1603.02735 (2016).
7. M. Khorasaninejad, W. T. Chen, R. C. Devlin, J. Oh, A. Y. Zhu, and F. Capasso, "Metalenses at visible wavelengths: Diffraction-limited focusing and subwavelength resolution imaging," *Science* **352**(6290), 1190–1194 (2016).
8. W. T. Chen, A. Y. Zhu, V. Sanjeev, M. Khorasaninejad, Z. Shi, E. Lee, and F. Capasso, "A broadband achromatic metalens for focusing and imaging in the visible," *Nat. Nanotechnol.* **13**(3), 220–226 (2018).
9. W. T. Chen, A. Y. Zhu, J. Sisler, Z. Bharwani, and F. Capasso, "A broadband achromatic polarization-insensitive metalens consisting of anisotropic nanostructures," *Nat. Commun.* **10**(1), 355 (2019).
10. V.-C. Su, C. H. Chu, G. Sun, and D. P. Tsai, "Advances in optical metasurfaces: fabrication and applications," *Opt. Express* **26**(10), 13148–13182 (2018).
11. A. M. Urbas, Z. Jacob, L. D. Negro, N. Engheta, A. D. Boardman, P. Egan, A. B. Khanikaev, V. Menon, M. Ferrera, N. Kinsey, C. DeVault, J. Kim, V. Shalaev, A. Boltasseva, J. Valentine, C. Pfeiffer, A. Grbic, E. Narimanov, L. Zhu, S. Fan, A. Alù, E. Pourtrina, N. M. Litchinitser, M. A. Noginov, K. F. MacDonald, E. Plum, X. Liu, P. F. Nealey, C. R. Kagan, C. B. Murray, D. A. Pawlak, I. I. Smolyaninov, V. N. Smolyaninova, and D. Chanda, "Roadmap on optical metamaterials," *J. Opt.* **18**(9), 093005 (2016).
12. C. Zhang, H. Subbaraman, Q. Li, Z. Pan, J. G. Ok, T. Ling, C.-J. Chung, X. Zhang, X. Lin, R. T. Chen, and L. J. Guo, "Printed photonic elements: nanoimprinting and beyond," *J. Mater. Chem. C* **4**(23), 5133–5153 (2016).
13. H.-H. Hsiao, C. H. Chu, and D. P. Tsai, "Fundamentals and applications of metasurfaces," *Small Methods* **1**(4), 1600064 (2017).
14. J. Bishop-Moser, C. Spadaccini, and C. Andres, "Metamaterials manufacturing: Pathway to industrial competitiveness," *Tech. rep.* (2018).
15. S. Barcelo and Z. Li, "Nanoimprint lithography for nanodevice fabrication," *Nano Convergence* **3**(1), 21 (2016).
16. J.-S. Park, S. Zhang, A. She, W. T. Chen, P. Lin, K. M. Yousef, J.-X. Cheng, and F. Capasso, "All-glass, large metalens at visible wavelength using deep-ultraviolet projection lithography," *Nano Lett.* **19**(12), 8673–8682 (2019).
17. S. V. Makarov, V. Milichko, E. V. Ushakova, M. Omelyanovich, A. Cerdan Pasaran, R. Haroldson, B. Balachandran, H. Wang, W. Hu, Y. S. Kivshar, and A. A. Zakhidov, "Multifold emission enhancement in nanoimprinted hybrid perovskite metasurfaces," *ACS Photonics* **4**(4), 728–735 (2017).
18. H. Wang, S.-C. Liu, B. Balachandran, J. Moon, R. Haroldson, Z. Li, A. Ishteev, Q. Gu, W. Zhou, A. Zakhidov, and W. Hu, "Nanoimprinted perovskite metasurface for enhanced photoluminescence," *Opt. Express* **25**(24), A1162–A1171 (2017).
19. Y. Yao, H. Liu, Y. Wang, Y. Li, B. Song, R. P. Wang, M. L. Povinelli, and W. Wu, "Nanoimprint-defined, large-area meta-surfaces for unidirectional optical transmission with superior extinction in the visible-to-infrared range," *Opt. Express* **24**(14), 15362–15372 (2016).
20. W. Chen, M. Tymchenko, P. Gopalan, X. Ye, Y. Wu, M. Zhang, C. B. Murray, A. Alu, and C. R. Kagan, "Large-area nanoimprinted colloidal au nanocrystal-based nanoantennas for ultrathin polarizing plasmonic metasurfaces," *Nano Lett.* **15**(8), 5254–5260 (2015).
21. A. T. Fafarman, S.-H. Hong, H. Caglayan, X. Ye, B. T. Diroll, T. Paik, N. Engheta, C. B. Murray, and C. R. Kagan, "Chemically tailored dielectric-to-metal transition for the design of metamaterials from nanoimprinted colloidal nanocrystals," *Nano Lett.* **13**(2), 350–357 (2013).
22. L. A. Ibbotson, A. Demetriadou, S. Croxall, O. Hess, and J. J. Baumberg, "Optical nano-woodpiles: large-area metallic photonic crystals and metamaterials," *Sci. Rep.* **5**(1), 8313 (2015).
23. Z. Wu and Y. Zheng, "Moiré metamaterials and metasurfaces," *Adv. Opt. Mater.* **6**(3), 1701057 (2018).
24. L. Gao, K. Shigeta, A. Vazquez-Guardado, C. J. Proglar, G. R. Bogart, J. A. Rogers, and D. Chanda, "Nanoimprinting techniques for large-area three-dimensional negative index metamaterials with operation in the visible and telecom bands," *ACS Nano* **8**(6), 5535–5542 (2014).
25. G. J. Sharp, S. I. Khan, A. Z. Khokhar, R. M. De La Rue, and N. P. Johnson, "Negative index fishnet with nanopillars formed by direct nano-imprint lithography," *Mater. Res. Express* **1**(4), 045802 (2014).
26. I. Bergmair, B. Dastmalchi, M. Bergmair, A. Saeed, W. Hilber, G. Hesser, C. Helgert, E. Pshenay-Severin, T. Pertsch, E. Kley, U. Hübner, N. H. Shen, R. Penciu, M. Kafesaki, C. M. Soukoulis, K. Hingerl, M. Muehlberger, and R. Schoefner, "Single and multilayer metamaterials fabricated by nanoimprint lithography," *Nanotechnology* **22**(32), 325301 (2011).
27. D. Franklin, Y. Chen, A. Vazquez-Guardado, S. Modak, J. Boroumand, D. Xu, S.-T. Wu, and D. Chanda, "Polarization-independent actively tunable colour generation on imprinted plasmonic surfaces," *Nat. Commun.* **6**(1), 7337 (2015).
28. B. D. Lucas, J.-S. Kim, C. Chin, and L. J. Guo, "Nanoimprint lithography based approach for the fabrication of large-area, uniformly-oriented plasmonic arrays," *Adv. Mater.* **20**(6), 1129–1134 (2008).
29. V. Rinnerbauer, E. Lausecker, F. Schäffler, P. Reiningger, G. Strasser, R. Geil, J. Joannopoulos, M. Soljačić, and I. Celanovic, "Nanoimprinted superlattice metallic photonic crystal as ultrasensitive solar absorber," *Optica* **2**(8), 743–746 (2015).

30. C. Zhang, Q. Li, L. Jin, X. Chen, and L. J. Guo, "Printed large-area flat optical component: Metasurfaces for cylindrical vector beam generation," in *2017 Conference on Lasers and Electro-Optics (CLEO)*, (IEEE, 2017), pp. 1–2.
31. G.-Y. Lee, J.-Y. Hong, S. Hwang, S. Moon, H. Kang, S. Jeon, H. Kim, J.-H. Jeong, and B. Lee, "Metasurface eyepiece for augmented reality," *Nat. Commun.* **9**(1), 4562 (2018).
32. G. Brière, P. Ni, S. Héron, S. Chenot, S. Vézian, V. Brandli, B. Damilano, J. Duboz, M. Iwanaga, and P. Genevet, "Semiconductors meta-optics: Fabrication and applications," in *CLEO: QELS_Fundamental Science*, (Optical Society of America, 2019), pp. FTh3M–7.
33. T. Hu, C.-K. Tseng, Y. H. Fu, Z. Xu, Y. Dong, S. Wang, K. H. Lai, V. Bliznetsov, S. Zhu, Q. Lin, and Y. Gu, "Demonstration of color display metasurfaces via immersion lithography on a 12-inch silicon wafer," *Opt. Express* **26**(15), 19548–19554 (2018).
34. Y. Dong, Z. Xu, N. Li, J. Tong, Y. H. Fu, Y. Zhou, T. Hu, Q. Zhong, V. Bliznetsov, S. Zhu, Q. Lin, D. H. Zhang, Y. Gu, and N. Singh, "Si metasurface half-wave plates demonstrated on a 12-inch cmos platform," *Nanophotonics* **9**(1), 149–157 (2019).
35. Z. Xu, Y. Dong, C.-K. Tseng, T. Hu, J. Tong, Q. Zhong, N. Li, L. Sim, K. H. Lai, Y. Lin, D. Li, Y. Li, V. Bliznetsov, Y.-H. Fu, S. Zhu, Q. Lin, D. H. Zhang, Y. Gu, N. Singh, and D.-L. Kwong, "Cmos-compatible all-si metasurface polarizing bandpass filters on 12-inch wafers," *Opt. Express* **27**(18), 26060–26069 (2019).
36. S. Colburn, A. Zhan, and A. Majumdar, "Varifocal zoom imaging with large area focal length adjustable metalenses," *Optica* **5**(7), 825–831 (2018).
37. Z. Zhang, J. Luo, M. Song, and H. Yu, "Large-area, broadband and high-efficiency near-infrared linear polarization manipulating metasurface fabricated by orthogonal interference lithography," *Appl. Phys. Lett.* **107**(24), 241904 (2015).
38. J. Luo, B. Zeng, C. Wang, P. Gao, K. Liu, M. Pu, J. Jin, Z. Zhao, X. Li, H. Yu, and X. Luo, "Fabrication of anisotropically arrayed nano-slots metasurfaces using reflective plasmonic lithography," *Nanoscale* **7**(44), 18805–18812 (2015).
39. K. Kim, G. Yoon, S. Baek, J. Rho, and H. Lee, "Facile nanocasting of dielectric metasurfaces with sub-100 nm resolution," *ACS Appl. Mater. Interfaces* **11**(29), 26109–26115 (2019).
40. S. Checcucci, T. Bottein, M. Gurioli, L. Favre, D. Grosso, and M. Abbarchi, "Multifunctional metasurfaces based on direct nanoimprint of titania sol–gel coatings," *Adv. Opt. Mater.* **7**(10), 1801406 (2019).
41. X. Wu, Y. Su, and J. Shi, "Perspective of additive manufacturing for metamaterials development," *Smart Mater. Struct.* **28**(9), 093001 (2019).
42. J. Cai, C. Zhang, C. Liang, S. Min, X. Cheng, and W.-D. Li, "Solution-processed large-area gold nanocheckerboard metasurfaces on flexible plastics for plasmonic biomolecular sensing," *Adv. Opt. Mater.* **7**(19), 1900516 (2019).
43. S.-J. Kim, M. Seong, H.-W. Yun, J. Ahn, H. Lee, S. J. Oh, and S.-H. Hong, "Chemically engineered au–ag plasmonic nanostructures to realize large area and flexible metamaterials," *ACS Appl. Mater. Interfaces* **10**(30), 25652–25659 (2018).
44. A. She, S. Zhang, S. Shian, D. R. Clarke, and F. Capasso, "Large area metalenses: design, characterization, and mass manufacturing," *Opt. Express* **26**(2), 1573–1585 (2018).
45. M. Kang, T. Feng, H.-T. Wang, and J. Li, "Wave front engineering from an array of thin aperture antennas," *Opt. Express* **20**(14), 15882–15890 (2012).
46. S. Wang, P. C. Wu, V.-C. Su, Y.-C. Lai, C. H. Chu, J.-W. Chen, S.-H. Lu, J. Chen, B. Xu, C.-H. Kuan, T. Li, S. Zhu, and D. P. Tsai, "Broadband achromatic optical metasurface devices," *Nat. Commun.* **8**(1), 187 (2017).
47. G. Hamdana, P. Puranto, J. Langfahl-Klabes, Z. Li, F. Pohlenz, M. Xu, T. Granz, M. Bertke, H. S. Wasisto, U. Brand, and E. Peiner, "Nanoindentation of crystalline silicon pillars fabricated by soft uv nanoimprint lithography and cryogenic deep reactive ion etching," *Sens. Actuators, A* **283**, 65–78 (2018).
48. S. Si and M. Hoffmann, "Consecutive imprinting performance of large area uv nanoimprint lithography using bi-layer soft stamps in ambient atmosphere," *Microelectron. Eng.* **176**, 62–70 (2017).
49. U. Plachetka, J. W. Kim, R. Khandelwal, H. Windgassen, C. Moormann, and H. Kurz, "Tailored etching processes for uv-nil resist material for si-antireflective surfaces," *Microelectron. Eng.* **110**, 361–364 (2013).
50. H. Schiff and A. Kristensen, "Nanoimprint lithography–patterning of resists using molding," in *Springer Handbook of Nanotechnology*, (Springer, 2010), pp. 271–312.
51. "Cryogenic etch re-emerges," <https://semiengineering.com/cryogenic-etch-re-emerges/>. Accessed: 2020-03-12.
52. M. Khorasaninejad and K. B. Crozier, "Silicon nanofin grating as a miniature chirality-distinguishing beam-splitter," *Nat. Commun.* **5**(1), 5386 (2014).